Beyond Constant Current: Origin of Pulse-Induced Activation in Phase-Transforming Battery Electrodes

Haitao D. Deng, Norman Jin, Peter M. Attia, Kipil Lim, Stephen D. Kang, Nidhi Kapate, Hongbo Zhao, Yiyang Li, Martin Z. Bazant, and William C. Chueh*

| Read Online

| ACCESS | | 📊 Metrics & More | | 📖 Article Recommendations | | 🔗 Supporting Information |

ABSTRACT: Mechanistic understanding of phase transformation dynamics during battery charging and discharging is crucial toward rationally improving intercalation electrodes. Most studies focus on constant-current conditions. However, in real battery operation, such as in electric vehicles during discharge, the current is rarely constant. In this work we study current pulsing in Li_XFePO_4 (LFP), a model and technologically important phase-transforming electrode. A current-pulse activation effect has been observed in LFP, which decreases the overpotential by up to ~70% after a short, high-rate pulse. This effect persists for hours or even days. Using scanning transmission X-ray microscopy and *operando* X-ray diffraction,

we link this long-lived activation effect to a pulse-induced electrode homogenization on both the intra- and interparticle length scales, i.e., within and between particles. Many-particle phase-field simulations explain how such pulse-induced homogeneity contributes to the decreased electrode overpotential. Specifically, we correlate the extent and duration of this activation to lithium surface diffusivity and the magnitude of the current pulse. This work directly links the transient electrode-level electrochemistry to the underlying phase transformation and explains the critical effect of current pulses on phase separation, with significant implication on both battery round-trip efficiency and cycle life. More broadly, the mechanisms revealed here likely extend to other phase-separating electrodes, such as graphite.

KEYWORDS: *LFP, pulse activation, solid solution, phase transformation, phase-field simulation*
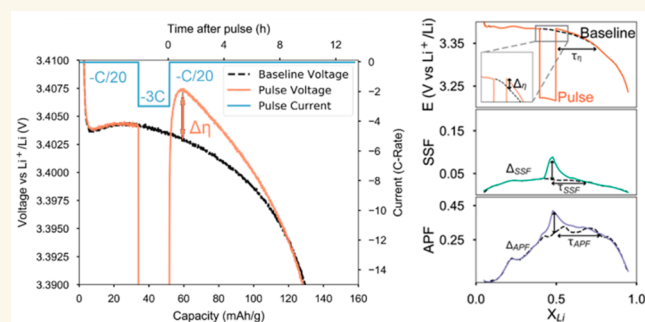
INTRODUCTION

Phase transformation is a key contributor to rate capability and cycle life of many technologically relevant Li-ion battery electrodes, such as Li_XFePO_4, $Li_{4\pm X}Ti_5O_{12}$, and graphite.[1−4] Accompanying phase transformation during battery operation is nonuniform current density, giving rise to current "hotspots" in the electrode, both within and between particles. Understanding these heterogeneities from the electrode down to the single-particle length scale during operation will allow for usage optimizations to improve battery performance and lifetime by leveraging the fundamental properties of phase-transforming electrodes. While much progress has been made to reveal the underlying dynamics of heterogeneities for batteries, most are focused on constant-current conditions. However, in real-world battery operation, fluctuating current profiles are common,[5−7] particularly during discharge. The link between current heterogeneities and electrode kinetics remains under-explored under such transient conditions. Moreover, past

works have seldom linked the observed heterogeneities to the current and voltage, which are the ultimate observables in batteries,[8−10] primarily because (i) the heterogeneity is linked to the phase transformation dynamics of a particle ensemble, which is complex (e.g., the metastable solid solution,[10−12] the particle-by-particle to concurrent intercalation,[13] the oscillation effect, etc.),[14] and (ii) a full understanding the transient dynamics of the electrode requires unified characterization and modeling of an ensemble of particles that quantify both single-particle behavior and multiparticle behavior, which is scarce in the current literature.
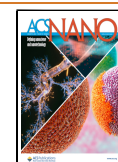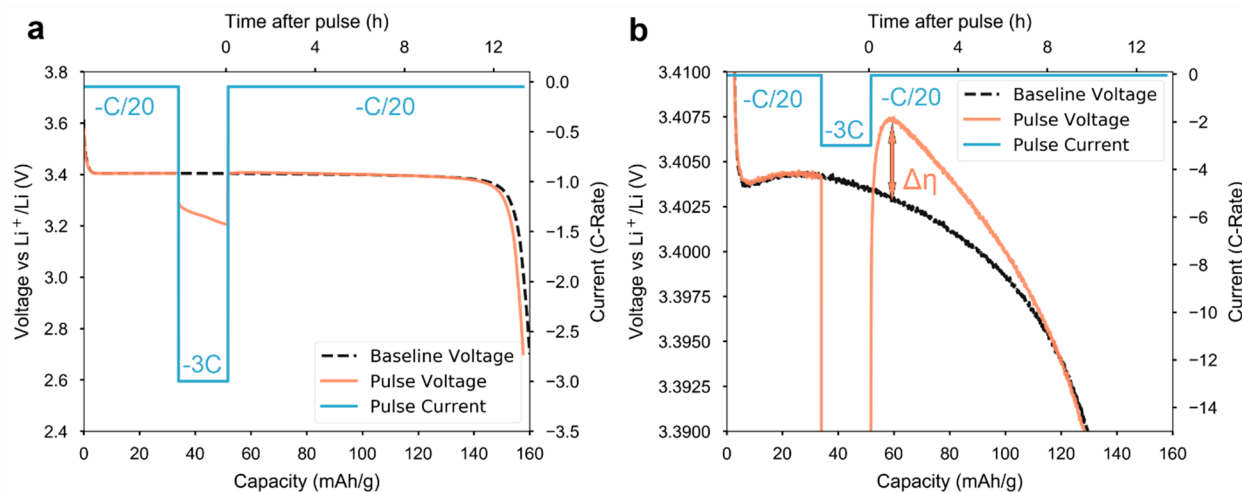
Figure 1. Pulse induced electrode activation. (a, b) The pulse experiment performed on an LFP microplatelet-Li half cell by conducting galvanostatic discharge in three successive steps: initial partial discharge at a C/20 base current to 80% SoC, pulsing at 3C (10% SoC), and finally discharge at C/20 to 2.7 V vs Li. In the voltage curve (orange) after pulsing we observe a decreased overpotential relative to the voltage curve at the same SoC obtained via a baseline C/20 discharge (black curve) with no pulse. (b) Magnification of the voltage axis. A reduction in overpotential, $\Delta\eta$, following the pulse is clearly seen. In (b) the current axis is also adjusted in scale for clarity. The observed difference in discharge capacity between the baseline and pulsed cell reflects sample-to-sample variation in cell fabrication. Figure S2 shows a follow-up experiment performing the pulse and baseline tests on the same cell, wherein the discharge capacity gap reduces to an insignificant value.

To address the first challenge, we simplify by looking at two important parameters that quantify the degree of current homogeneity in phase-separating electrodes: active particle fraction (APF) and solid solution fraction (SSF).[8,12,13] Both contribute to a low electrochemical resistance when their values are high due to a high homogeneity and hence high electrochemically active surface. APF quantifies the fraction of particles in the electrode that are experiencing current at a given time. In phase-separating electrodes, individual particles exhibit dramatically different current densities[8,9,15] relative to the value averaged across the electrode. At low (dis)charge rates, only a small fraction of particles is active, compared to a larger fraction at higher rates.[13] SSF quantifies the fraction of the thermodynamically forbidden but kinetically stabilized solid solution in the miscibility gap.[11,16−19] Experiment and theory suggest that at high global current densities phase-separating electrodes can proceed via a solid solution pathway instead of a moving boundary, phase-separating pathway.[10,15,17,18,20] Importantly, many phase-transforming electrodes at an intermediate state-of-charge (SoC) exhibit a higher reaction rate constant than the end-member phases, as confirmed by both theory and experiment.[9]

To address the second challenge, we investigate the dynamic phase separation behavior of Li_XFePO_4 (L_XFP, $0 < X < 1$) on both the particle and electrode length scales during current pulses by employing advanced characterization and many-particle phase-field modeling. We select LFP as a model system to study phase transformation because of its industrial relevance,[21] well-characterized properties,[22−25] and wide miscibility gap.[26−29] Extensive work focused on understanding both the thermodynamics[18,29] and kinetics[13,17,18] of LFP has helped explain its high rate performance and cycle life, despite mechanical stress imposed by phase transformation.[18,30,31] Recently, Moškon et al.[32] and Katrašnik et al.[33] discovered an activation effect (i.e., a decrease of the overpotential) in LFP electrodes during pulsed charging and discharging. This effect persists long after the pulse has ended, in some cases, for tens

of hours. We directly connect these electrochemical observations to dynamics at the electrode and particle length scales. Combining X-ray spectro-microscopy and *operando* X-ray diffraction, we observed substantial increases in APF and SSF following the pulse. Using phase-field simulations, we reproduced these observations and separated the contributions due to APF and SSF following the pulse. Our investigation into transient effects establishes a deeper understanding of battery kinetics under real-world, beyond-constant-current conditions and enables optimization of surface diffusion and pulse (dis)charge rates to leverage kinetic activation.

RESULTS AND DISCUSSION

Pulse-Induced Electrode Activation. To study the non-steady-state behavior of an LFP electrode, we apply a single constant-current pulse in the miscibility gap of LFP. Figure 1a,b shows a typical pulse experiment on LFP platelets during lithiation (discharge) with a baseline current (I_{base}) of −C/20 and a pulse current (I_{pulse}) of −3C, where 1C = 150 mA g^{-1}. See the synthesis protocol and characterization in the Supporting Information. The measured voltage curve of the pulse experiment (orange line) is shown together with the baseline voltage curve without the pulse (black line). Before the pulse, the two voltage curves are identical. After the pulse, the voltage profile of the pulsed cell departs from that of the baseline cell (Figure 1b). We designate the magnitude of decrease in the total overpotential as $\Delta\eta$. The pulse lowers the lithiation overpotential by as much as 70% for ∼8 h following the pulse. This finding indicates that the physical mechanism underlying the pulse activation process has a long relaxation time constant. We also performed the pulsing experiment in a three-electrode cell (Figure S1), which confirms that the activation does not result from the lithium metal counter electrode.

We observed similar pulse-induced overpotential reductions across different cycling conditions and particle morphologies. Figure S3 compares the overpotential reduction for a
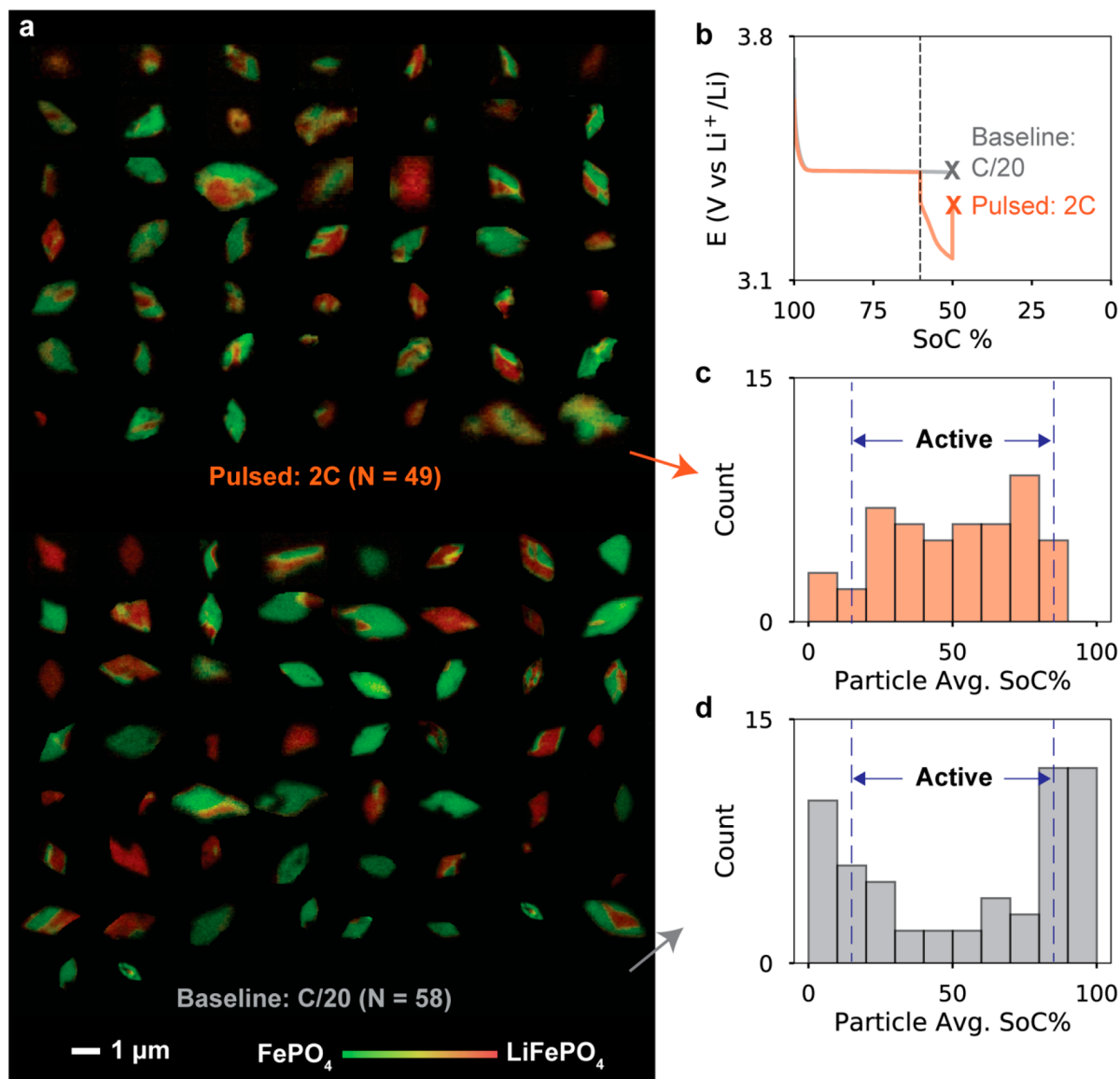
Figure 2. Scanning transmission X-ray microscopy (STXM) of a microplatelet electrode with and without pulsing. (a) STXM data set of 107 particles harvested from electrodes at 50% SoC. Two samples were prepared: "Pulsed" and "Baseline". (b) "Baseline" was discharged at C/20 from 100% to 50% SoC. "Pulsed" was similarly discharged to 50% SoC, and a 2C current pulse was applied between 60% and 50% SoC (3 min pulse). Both Baseline and Pulsed were disassembled at 50% SoC. Note: the voltage curve for the Pulsed sample ends below that of the Baseline due to the last point not being registered by the potentiostat. The overpotential had approximately returned to the steady-state value at the end of the pulse. (c and d) Distribution of particle SoC for Pulsed and Baseline, respectively. We see a bimodal distribution of particles in the Baseline sample with peaks near 100% SoC and 0% SoC, while the Pulsed sample contains a much higher fraction of particles at intermediate SoCs.

commercial LFP powder synthesized via solid-state reactions and two additional powders synthesized via solvothermal reaction. The activation effect is robust across these particle morphologies, with the exception of nanoparticle LFP, which shows a negligible activation effect due to the nucleation length scale. We will return to this observation in a later section after discussing the physical origin of the activation. The overpotential reductions are comparable with the original reports by Moškon et al.[32] and Katrašnik et al.[33]

Physical Characterization of Pulsing Electrodes. To understand the pulse activation effect, we quantify how APF and SSF are modified by and evolve after the current pulses. Scanning transmission X-ray microscopy (STXM) is used to map the SoC of LFP at the single-particle level (Figure

2a).[8,9,13] The cycling and pulse profiles are shown in Figure 2b. We examined a −C/20 lithiation (discharge) interrupted by a −2C pulse beginning at 60% SoC and ending at 50% SoC ("Pulsed"). We also examined a baseline at the same current without the pulse ("Baseline").

Upon reaching 50% SoC, both cells were disassembled, and the electrodes were rinsed with dimethyl carbonate, dried within a few minutes of the current being stopped, and then stored under Ar. Our previous work shows interparticle phase separation happens in ~8 h of exposure to electrolyte, and interparticle phase separation occurs even slower.[9] Thus, we are confident this procedure prevents the redistribution of lithium between particles and slows lithium migration within a single particle.
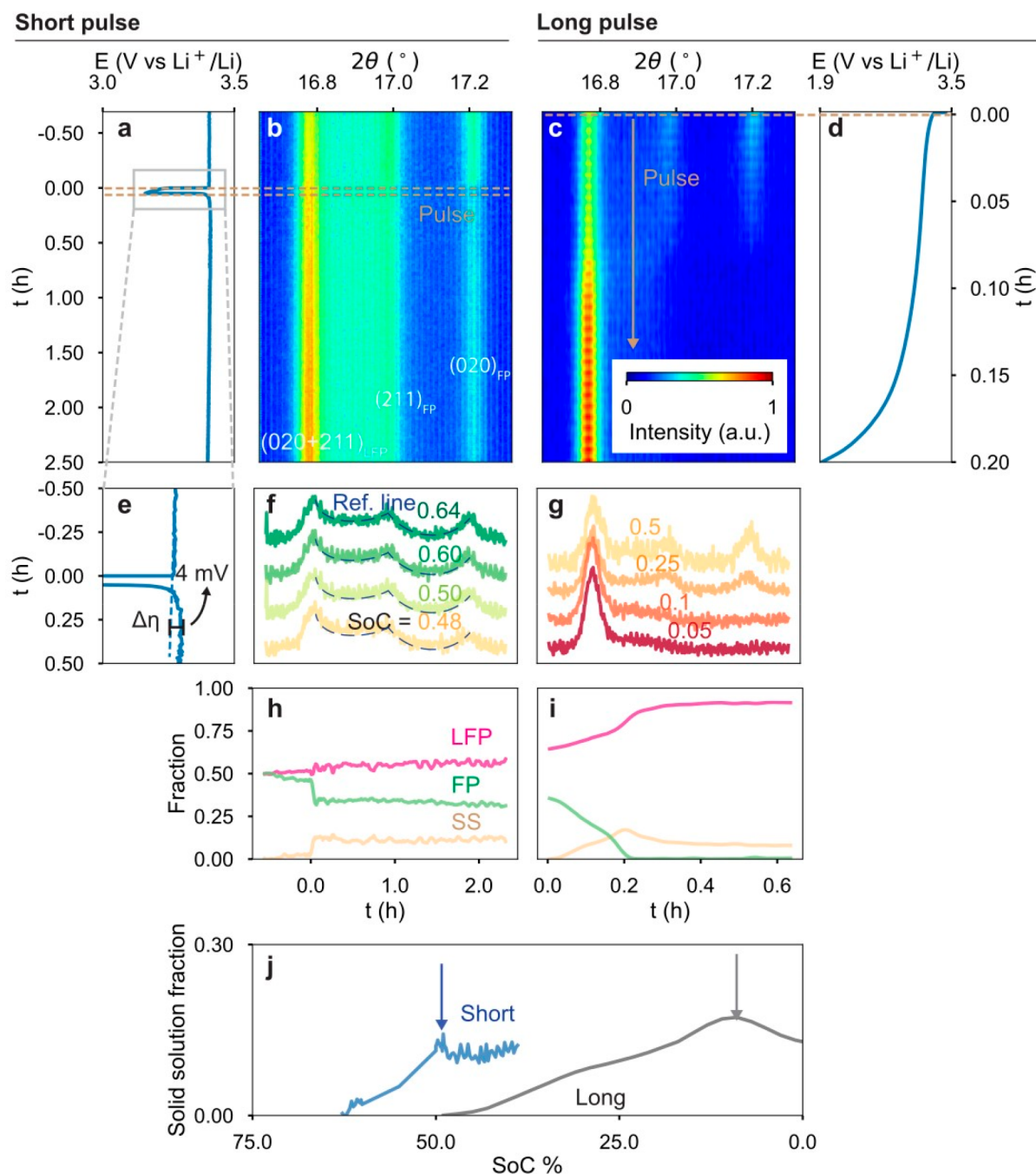
Figure 3. *Operando* X-ray diffraction. (a) Electrochemistry profile of pulsing experiments. Conditions of the short pulse were identical to those of the Pulsed sample from the STXM experiment (60% to 50% SoC, 2C rate). (b) Waterfall plot showing the evolution of the synchrotron X-ray diffraction pattern over the course of the short pulsing experiment. X-ray wavelength is 0.8856 Å. (c, d) The experiment was repeated with a long pulse (50% to 0% SoC). For the long pulse experiment, diffraction data were taken from the start of the pulse to the end of discharge. The oscillations visible in the spectra are due to a low temporal resolution. We limited the number of diffraction patterns measured to reduce the extent of beam damage to the sample. (e) A zoomed-in region of the voltage profile showing overpotential reduction during the short pulse experiment. (f, g) Line-cuts of the diffraction patterns. The dashed reference lines are a guide for comparing line cuts to the beginning of the pulse (64% SoC). (h) Phase fractions within the electrode before, during, and after pulsing observed by *operando* XRD. $t = 0$ indicates the beginning of the pulse. LFP indicates the lithiated phase, FP indicates the delithiated phase, and SS indicates intermediate solid-solution phases. (i) Phase fraction evolution during the long pulse. (j) Comparison of the solid-solution evolution of the short and long pulses, showing consistent growth rates of SSF between the two experiments. During the short pulse SSF peaks at 10% SSF, while in the long pulse SSF peaks at 18%. This demonstrates the slow speed of solid-solution formation in LFP.

The average pixel-weighted SoC of the baseline data was 54.2%, and the average SoC of the pulse data was 50.1%, which is consistent with the 50% SoC from electrochemistry. From the single-particle SoC maps, we calculated the average SoC for each individual particle. Figure 2c,d presents particle-count histograms of the "Pulsed" and "Baseline" electrodes as a function of SoC for a collection of particles (N = 49 and 58, respectively). The "Pulsed" electrode shows a majority of
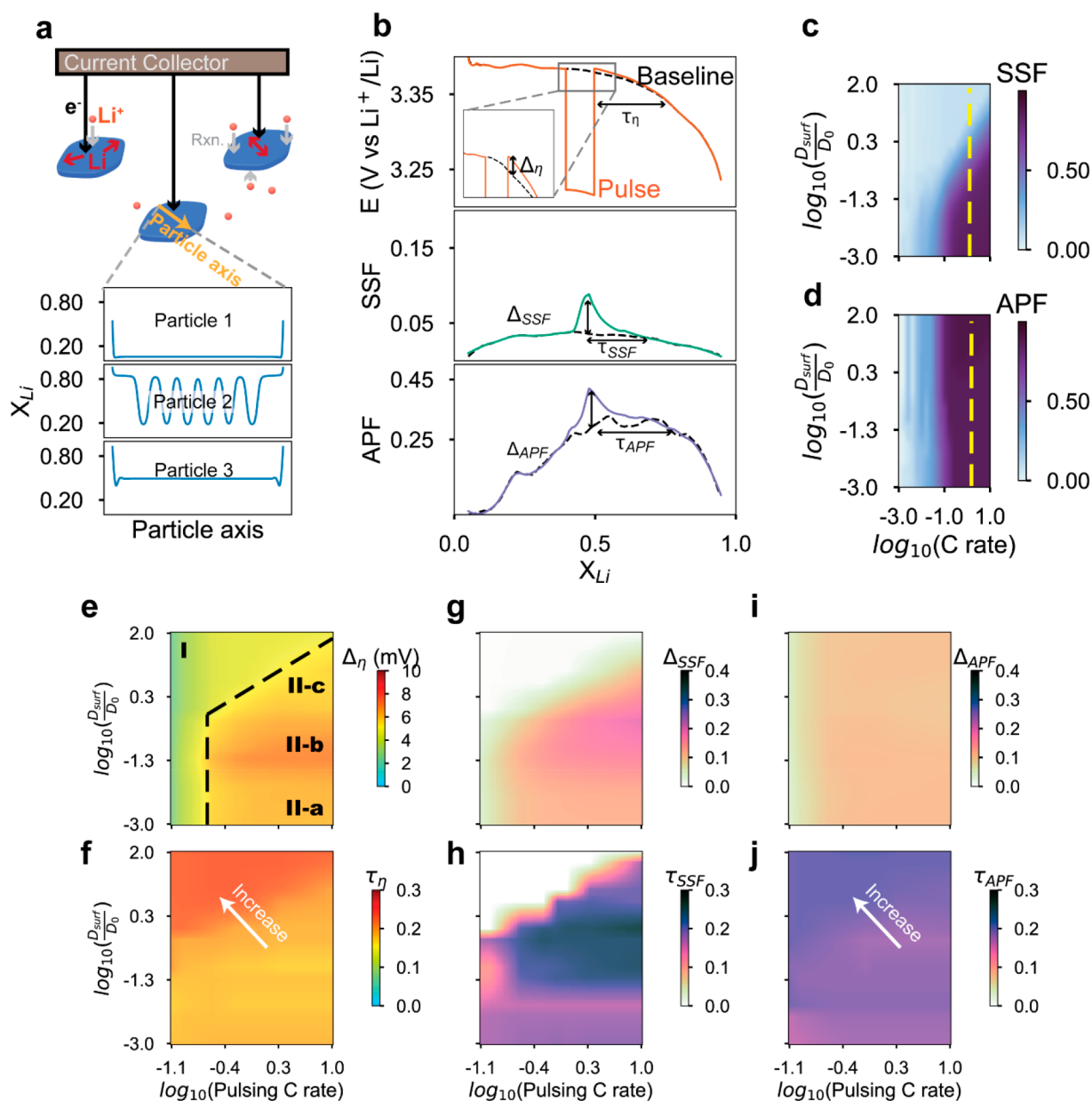
Figure 4. Many-particle phase-field electrode simulation. (a) Schematic of many-particle phase field simulation. We illustrate three cases of intercalation behavior: inactive particle (particle 1), low SSF and low APF, phase-separated particle (particle 2), low SSF and high APF, and solid solution particle (particle 3), high SSF and high APF. Formation of the interface is perpendicular to the particle axis. (b) A typical 100-particle phase-field simulation showing voltage, APF, and SSF. Baseline current is C/20, and pulse magnitude is 2C spanning from X = 0.4 to 0.5. (c, d) Parametric APF and SSF maps for constant-current discharge at X = 0.5. Dashed line is the baseline (C/20) we compare to for pulsing simulations. (e−j) Magnitude and effective lifetime (in units of SoC span) of overpotential reduction (e, f), SSF change (g, h), and APF change (i, j). Electrode activation is divided into two regimes based on the SSF change. In regime I, SSF = 0, APF dominates the activation effect. In regime II, both APF and SSF contribute to the activation effect, while the activation lifetime is dominantly characterized by the excess SSF lifetime. Comparison of effective lifetime suggests stronger correlation between activation effect and APF, as both increase with higher surface diffusivity and smaller C-rate (f, h, j). D_0 = 6.25 × 10^{-12} cm^2·s^{-1}, 1C is 5.4 × 10^{-3} A·m^{-2}.

particles at intermediate Li compositions inside the miscibility gap, and the histogram exhibits a unimodal distribution (Figure 2c). In contrast, the "Baseline" electrode clearly shows a bimodal distribution of SoC with most particles being at either high or low SoC, consistent with past low-rate constant current cycling (Figure 2d). Specifically, we define an active particle as a particle with an SoC between 15% and 85%; under this definition, the "Pulsed" sample shows an APF of 90% and the "Baseline" sample shows an APF of 40%. This difference is notable not only because of its magnitude but also

the rate at which such a large change develops (−2C pulse was only applied for 3 min). This large increase in the APF upon pulsing is insensitive to the selected SoC thresholds (15% and 85%) defining active particles, as demonstrated in Figure S4.

Although increasing APF with pulsing is consistent with a lowered reaction overpotential, the solid-solution fraction could also contribute. In principle, a larger SSF gives a higher exchange current density at intermediate compositions of L$_X$FP. As established in the literature, LFP contains minimal amounts of solid solution during low rates of discharge.[10,17,34]

To quantify SSF, we tracked the phase behavior of microplatelet LFP during the pulse via *operando* X-ray diffraction (Figure 3). Electrode disks sampled from the same electrode sheet used in the STXM study were fabricated into single-layer pouch cells and cycled in an identical manner. The quantification of the phase fraction is detailed in the Methods section of the Supporting Information. Figure 3e shows the overpotential reduction with pulsing peaks at 4 mV, consistent with the results shown in Figure 1. Figure 3h shows the phase fraction of the (1) lithiated LFP phase, (2) delithiated FP phase, and (3) solid solution. An SSF of 3% was observed before the pulse, which increased to 13% during the short 3 min pulse. We also conducted *operando* XRD with a longer, 15 min pulse at the same pulse magnitude (i.e., from 50% to 0% SoC); Figure 3c,d,i show the evolution of the diffraction patterns, electrochemistry, and fitted phase fractions for the longer pulse experiment, respectively. The SSF steadily increases to 18% over 15 min, at which point the SSF begins to decrease as the electrode completes its transformation to the LFP phase. Note, as this longer pulse did not start at the same SoC as in the first experiment, a difference in the SSF formation speed is expected, which we observe.

The long time constant of solid-solution formation and relaxation is notable as compared with previous *operando* X-ray diffraction results on LFP performed under a constant current.[10] We postulate that this difference is explained by two factors. First, our large microplatelet LFP rather than nanoparticles (as used previously[10,35]) are much less rate-capable as a result of size-dependent L_XFP kinetics.[25,35,36] Second, our pulse current was an order of magnitude smaller than the 60C previously adopted by Wagemaker et al.;[10] therefore the driving force toward the solid solution is much lower. The combination of these two factors likely explains the observed differences in the solid-solution evolution speed.

We now address the apparent discrepancy in the magnitude of the pulse activation between nanoparticle LFP and the larger particle morphologies shown in Figure S3. Nanoparticle LFP thermodynamically follows a solid-solution pathway due to surface energy considerations and the particle size approaching the nucleation length scale,[29,37−39] which also leads to a very high APF during particle lithiation. As these nanoparticles already exhibit high APF and SSF even during low-rate discharge, high-current pulsing does not further activate the electrode.

Summarizing, we observe that current pulsing substantially increases the APF from 40% to 90% APF and increases the SSF from 3% to 13%. From the magnitude of these increases alone, we cannot straightforwardly estimate which of the two contributes more strongly to the overpotential reduction, as the relationship between SSF/APF and the electrochemical resistance is complex due to the nonlinear and dynamical governing equation.[1,8,9,20,40]

Multiparticle Phase-Field Simulations of Electrode Activation. To further investigate the origin of the electrode activation effect and to mechanistically deconvolve SSF from APF, we simulated a 100-particle electrode using a phase-field model. For LFP electrodes, phase-field simulation has been crucial in understanding intercalation pathways, reaction kinetics, dynamics, and strain, and thus is an important approach to understanding the electrode activation mechanism.[4,10,14,17,18,41] A detailed description of the model formulation and parameters is provided in the Supporting Information section "Numerical phase-field porous-electrode

simulations". Briefly, the governing equation of the multiparticle system is

$$\frac{\partial X^i}{\partial t} = -\nabla \cdot J_D^i + R^i(X^i, \eta^i) + \xi^i, \, i = 1, 2, 3, ..., N \quad (1)$$

where X is the spatially resolved Li composition within the particle; t is the time; J_D is the effective in-plane diffusional current density flux, which is proportional to the surface diffusivity D_{surf}; η is the electrochemical reaction overpotential at the LFP/carbon coating/electrolyte triple-phase boundary; ξ is the Langevin noise that represents thermal fluctuation; the superscript i is the particle index; and N is the total number of particles. Within each particle, the local Li composition is simulated on a one-dimensional particle axis, where the Li composition profile is driven by both the out-of-plane surface reaction R and the in-plane surface diffusion J_D, as shown in Figure 4a, consistent with previous work.[9] The evolution of the equation is constrained by the total current of the electrode:

$$I = e\rho_s \sum_i \int_0^{L^i} \frac{\partial X^i}{\partial t} dr \quad (2)$$

where e is the elemental charge, ρ_s is the volumetric lithium site concentration density, and L is the particle size. The model captures many behaviors in phase-separating electrodes (e.g., Li_XFePO_4) such as voltage hysteresis, rate-dependent intercalation pathways, suppression of phase separation under high current, and surface-diffusion-controlled intraparticle phase separation.[8,9,13,17,42,43] We simulated both the baseline and the pulsing experiments and reproduced the activation effect in the voltage curves (Figure 4b).

As discussed earlier, the electrode activation effect is a convolution of increased APF and SSF with pulsing. In the baseline, non-pulsed simulation presented in Figure 4c,d, we observe two major trends in the APF and SSF: (1) C-rate increases both APF and SSF, while (2) surface diffusion suppresses the formation of solid solution but has no effect on APF. This result is consistent with our previous work.[8,9] In the pulsing simulation, we generated parametric maps of the overpotential reduction (at 50% SoC) ($\Delta\eta$) and the characteristic lifetime ($\tau_{\Delta\eta}$, defined as the span of Li composition over which the overpotential change had decreased to 20% of the onset value) over different pulse magnitudes (I) and surface diffusivities (D_{surf}). The results are presented in Figure 4e,f. We similarly compute the magnitude and characteristic lifetime of the increase in SSF (ΔSSF, τ_{SSF}) and APF (ΔAPF, τ_{APF}) with pulsing, as shown in Figure 4g−j.

Two Regimes of Activation. Our pulsing simulations reveal two regimes, outlined in Figure 4e. In regime I, ΔSSF is negligible (high D_{surf}, low I); in regime II, both SSF and APF are elevated (low D_{surf}, high I) (Figure 4g,i). Previous theoretical and experimental studies[9,17] have shown that a critical local current density divides the thermodynamically favorable phase-separation regime and the kinetically controlled quasi-solid-solution regime, outlined in Figure 4c. Here, we can see that a similar effect occurs under pulsing, where a critical pulsing current separates the regimes of substantial and negligible homogenization via an increase in SSF.

In regime I, the solid solution is unstable because of fast surface diffusion. Therefore, SSF is not activated by the pulse. Instead, the activation effect is dominated by the APF in terms of both magnitude and effective lifetime. A simplified model using traveling waves detailed in the Supporting Information

demonstrates a linear scaling between $\Delta\eta$ and $\Delta\left(\frac{1}{\text{APF}}\right)$. This result highlights the importance of attaining concurrent intercalation across many particles (i.e., high APF) for energy efficiency.

In regime II, once the local current density exceeds the critical threshold, both SSF and APF lower the overpotential. In the scenario where particles undergo a particle-by-particle solid-solution pathway at the baseline current, pulse activation exists in the parameter space explored (region II-a: low D_{surf}, high C-rate pulse), with a linear scaling relation observed between $\Delta\eta$ and $\Delta\left(\frac{1}{\text{APF}}\right) = \Delta\left(\frac{1}{\text{SSF}}\right)$. See the additional discussions in the Supporting Information. Moving up across the parametric space (region II-b: increasing D_{surf}, fixed C-rate), we observe that ΔSSF increases until it is maximized at intermediate ranges while ΔAPF remains constant. Correspondingly, the magnitude of $\Delta\eta$ is maximized. This maximization in ΔSSF and ΔAPF is also consistent with previous studies, where maximization is reached because of the limited number of available Li sites to react.[44] As we further increase D_{surf} while fixing the C-rate (region II-c), ΔSSF decreases due to accelerated surface Li diffusion, and $\Delta\eta$ decreases accordingly. The result indicates that electrode activation can be maximized at intermediate surface Li diffusivity.

We now turn our attention toward the characteristic lifetime of pulse activation. To ensure generalization, we study the lifetime under various decay thresholds, defined as the ratio between the initial excess SSF and the final SSF. By plotting the characteristic times of overpotential reduction, APF, and SSF against one another (Figure S8), we find that the characteristic lifetime of the activation effect correlates with excess APF characteristic lifetime, but not excess SSF characteristic lifetime. This suggests that the longevity of the activation is dependent only on the number of additional particles activated and not on the development of a solid solution. However, the initial magnitude of the activation correlates with the sum of ΔSSF and ΔAPF. This finding highlights an important distinction between the roles of inter- and intraparticle homogeneity during pulse activation: although increasing either aspect of uniformity boosts the electrode kinetics, only homogenization on the electrode scale induces a lasting improvement. This implies slower reaction kinetics associated with relaxation of interparticle heterogeneity compared to intraparticle Li redistribution. Additionally, pulse activation exhibiting low APF and high SSF means that the activation is confined to a small number of active particles. The activation effect will consequently fade quickly when those few particles complete discharge. We note that the 1D phase-field simulation may overestimate the lifetime of SSF due to the lack of a surface curvature effect that speeds up relaxation kinetics (details discussed in future work). Nonetheless, we believe the strong correlation between the activation lifetime and APF remains justified.

Our simulation results have many implications for battery cycling under realistic, non-constant-current conditions. Our previous work suggested that minimizing the surface diffusivity of LFP through electrolyte/surface engineering leads to optimal electrode kinetics.[9] Here, we present alternative strategies via pulsing, leveraging the intermediate surface Li diffusion regime shown in Figure 4e (II-b) for maximum activation effectiveness. Similarly, pulsing can also minimize the phase-transformation-induced interfacial strain that leads to electrode degradation. More generally, we hope that this work inspires further innovations in optimizing electrode kinetics for non-steady-state conditions and maximizing cycle life.

CONCLUSIONS

We reveal the mechanisms that underlie the recently discovered pulse activation phenomenon in LFP battery electrodes. The activation persists for many hours under slow galvanostatic discharge conditions after pulsing and results in an up to 70% decrease in the electrode overpotential. Our physical characterization links this effect to an increased homogeneity within the electrode at both the intra- and interparticle length scales. Many-particle phase-field simulations reinforce this finding, indicating that for reasonable surface diffusivities and moderate to high pulse currents short-term activation is facilitated both by an increase in the solid-solution fraction within the LFP particles and by an increase in the active particle fraction throughout the electrode. Although the solid solution relaxes via surface diffusion, the increased APF with pulsing is sustained for an extended period, rationalizing the longevity of the activation under slow galvanostatic discharge following the pulse. We correlate the observed decrease in overpotential to dynamics in the electrode at both the inter- and intraparticle level upon pulsing.

These findings may inform rational electrode design and control through material properties (e.g., surface Li diffusivity) to maximize the electrode-level kinetics. Furthermore, computational models of phase-transforming electrodes should account for these effects when simulating non-galvanostatic conditions. The practical implications of this effect are also significant: heuristics using voltage measurement to determine state-of-charge or state-of-health should account for the possible effects of past current pulses. Likewise, battery management systems can exploit this effect to offer faster battery charging and discharging to consumers. For example, following a burst of regenerative braking current, an electric vehicle can charge more quickly than anticipated due to pulse activation. While it is possible that applying these high current pulses repeatedly to the electrode could cause accelerated degradation, since these high overpotentials will also induce a solid solution in LFP particles, the pulse will reduce the amount of material experiencing interfacial strain. This should mitigate potential damage to the particles during pulse cycling. We also believe that the observed kinetic stabilization of high SSF and APF under transient conditions is a key factor explaining the fast kinetics of LFP in practical use.

History-dependent properties of phase-transforming electrodes are very general and by no means limited to Li-ion batteries. For example, similar voltage overshoots are observed in carbon-monofluoride/silver−vanadium oxide (CF_x/SVO) primary batteries used in implantable medical devices, when sudden changes in current are applied.[45] More complex history-dependent voltage responses (not only simple pulses) have been explained quantitatively in terms of active particle fractions by hybrid multiphase porous electrode theory (MPET) simulations, which generalize the phase-field model used here. We hope this understanding of phase-transforming electrode behavior will encourage further studies under nongalvanostatic conditions,[46] leading to more accurate mathematical models and to optimizations in everyday usage of batteries containing phase-transforming materials.

METHODS

Synthesis & Cell Assembly. The LiFePO$_4$ microplatelets that were used in both the STXM and XRD experiments were solvothermally synthesized in a Berghof BR-100 reactor with a Teflon lining using a stoichiometric 1:1:1 ratio of LiOH, FeSO$_4$, and H$_3$PO$_4$ in a 40−60 ratio of PEG-400 to water at 140 C for 6 h, then 180 °C for 18 h under an inert atmosphere. All reagents were sourced from Sigma-Aldrich. The powder was subsequently washed by DI water and isopropyl alcohol, dried, and annealed at 600 °C for 5 h in inert atmosphere with sucrose to reduce defect concentration and apply a thin layer of carbon coating. The powder was subsequently mixed into a slurry with Super-P carbon black and PVDF binder at a mass ratio of 74:20:6. This slurry was then blade-casted onto coated aluminum foil to a final thickness of ∼50 μm and assembled into cells. The loading of the electrodes was approximately 2.1 mg/cm^2.

The nanoparticle LFP was synthesized by using the same method as above. The only difference was the solvent (ethylene glycol) and the reaction temperature (180 °C for 24 h).

Electrochemical Tests. The two-electrode electrochemical measurements reported were performed using Hohsen 2016 and 2032 coin cells in a controlled temperature chamber at 30 ± 1 °C. The electrolyte used was 150 μL of 1 M LiPF$_6$ in 1:1 EC/DMC or 1:1 EC/DEC. Before use, the LFP-Li cells were precycled using the following protocol: 3 full C/10 charge and discharge cycles, followed by 3 C/5 full cycles, 3 1C full cycles, and eventually 2C full cycles. The voltage cutoffs were set at 2 and 4 V. Two-electrode tests were performed by an Arbin LBT20084 battery cycler or a Biologic BCS-805. Three-electrode cells were fabricated as detailed in Kuo et al.[47] Three-electrode measurements were performed using a Biologic MPG-2.

ASSOCIATED CONTENT

(si) Supporting Information

The Supporting Information is available free of charge at https://pubs.acs.org/doi/10.1021/acsnano.3c09742.

Additional electrochemical pulse data, details of STXM and XRD analysis techniques, extensive description of phase-field model (PDF)

AUTHOR INFORMATION

Corresponding Author

William C. Chueh − *Department of Materials Science and Engineering, Stanford University, Stanford, California 94305, United States; Stanford Institute for Materials & Energy Sciences, SLAC National Accelerator Laboratory, Menlo Park, California 94025, United States;* orcid.org/0000-0002-7066-3470; Email: wchueh@stanford.edu

Authors

Haitao D. Deng − *Department of Materials Science and Engineering, Stanford University, Stanford, California 94305, United States;* orcid.org/0000-0003-3225-4219

Norman Jin − *Department of Materials Science and Engineering, Stanford University, Stanford, California 94305, United States*

Peter M. Attia − *Department of Materials Science and Engineering, Stanford University, Stanford, California 94305, United States;* orcid.org/0000-0003-4745-5726

Kipil Lim − *Department of Materials Science and Engineering, Stanford University, Stanford, California 94305, United States; Stanford Institute for Materials & Energy Sciences, SLAC National Accelerator Laboratory, Menlo Park, California 94025, United States*

Stephen D. Kang − *Department of Materials Science and Engineering, Stanford University, Stanford, California 94305, United States*

Nidhi Kapate − *Department of Materials Science and Engineering, Stanford University, Stanford, California 94305, United States*

Hongbo Zhao − *Department of Chemical Engineering, Massachusetts Institute of Technology, Cambridge, Massachusetts 02139, United States*

Yiyang Li − *Department of Materials Science and Engineering, Stanford University, Stanford, California 94305, United States;* orcid.org/0000-0002-5809-6901

Martin Z. Bazant − *Department of Chemical Engineering, Massachusetts Institute of Technology, Cambridge, Massachusetts 02139, United States; Department of Mathematics, Massachusetts Institute of Technology, Cambridge, Massachusetts 02139, United States;* orcid.org/0000-0002-8200-4501

Complete contact information is available at:
https://pubs.acs.org/10.1021/acsnano.3c09742

Author Contributions

N.J. and Y.L. synthesized the platelet particles and nanoparticles. N.K. and S.D.K. performed the three-electrode measurements and capacity checks. P.M.A. and N.J. performed the STXM characterization. P.M.A. analyzed the STXM result. K.L. designed the operando diffraction holder. H.D.D., N.J., and K.L performed the operando diffraction. H.D.D. analyzed the XRD data. N.J. performed the relaxation experiment. H.D.D. performed the phase-field simulations. H.Z. and M.Z.B. provided input to the simulations of LFP. All the authors contributed to the discussion of the results and writing of the manuscript. H.D.D. and N.J. contributed equally to this work.

Notes

The authors declare no competing financial interest.

REFERENCES

(1) Ferguson, T. R.; Bazant, M. Z. Phase Transformation Dynamics in Porous Battery Electrodes. *Electrochim. Acta* **2014**, *146*, 89−97.

(2) Verde, M. G.; et al. Elucidating the Phase Transformation of Li$_4$Ti$_5$O$_{12}$ Lithiation at the Nanoscale. *ACS Nano* **2016**, *10*, 4312−4321.

(3) Funabiki, A.; Inaba, M.; Abe, T.; Ogumi, Z. Stage Transformation of Lithium Graphite Intercalation Compounds Caused by Electrochemical Lithium Intercalation. *J. Electrochem. Soc.* **1999**, *146*, 2443−2448.

(4) Smith, R. B.; Bazant, M. Z. Multiphase Porous Electrode Theory. *J. Electrochem. Soc.* **2017**, *164*, E3291−E3310.

(5) Baure, G.; Dubarry, M. Synthetic vs. Real Driving Cycles: A Comparison of Electric Vehicle Battery Degradation. *Batteries* **2019**, *5*, 42.

(6) Brady, J.; O'Mahony, M. Modelling charging profiles of electric vehicles based on real-world electric vehicle charging data. *Sustain. Cities Soc.* **2016**, *26*, 203−216.

(7) Devie, A.; Vinot, E.; Pelissier, S.; Venet, P. Real-world battery duty profile of a neighbourhood electric vehicle. *Transp. Res. Part C Emerg. Technol.* **2012**, *25*, 122−133.

(8) Lim, J.; et al. Origin and hysteresis of lithium compositional spatiodynamics within battery primary particles. *Science* **2016**, *353*, 566−571.

(9) Li, Y.; et al. Fluid-enhanced surface diffusion controls intraparticle phase transformations. *Nat. Mater.* **2018**, *17*, 915−922.

(10) Zhang, X.; et al. Rate-Induced Solubility and Suppression of the First-Order Phase Transition in Olivine LiFePO$_4$. *Nano Lett.* **2014**, *14*, 2279−2285.

(11) Liu, H.; et al. Capturing metastable structures during high-rate cycling of LiFePO$_4$ nanoparticle electrodes. *Science* **2014**, *344*, 1252817−1252817.

(12) Hess, M.; Sasaki, T.; Villevieille, C.; Novák, P. Combined operando X-ray diffraction-electrochemical impedance spectroscopy detecting solid solution reactions of LiFePO$_4$ in batteries. *Nat. Commun.* **2015**, *6*, 8169.

(13) Li, Y.; et al. Current-induced transition from particle-by-particle to concurrent intercalation in phase-separating battery electrodes. *Nat. Mater.* **2014**, *13*, 1149−1156.

(14) Li, D.; et al. Electrochemical Oscillation in Li-Ion Batteries. *Joule* **2018**, *2*, 1265−1277.

(15) Owen, J.; Hector, A. Phase-transforming electrodes. *Science* **2014**, *344*, 1451−1452.

(16) Sharma, N.; et al. Direct Evidence of Concurrent Solid-Solution and Two-Phase Reactions and the Nonequilibrium Structural Evolution of LiFePO$_4$. *J. Am. Chem. Soc.* **2012**, *134*, 7867−7873.

(17) Bai, P.; Cogswell, D. A.; Bazant, M. Z. Suppression of Phase Separation in LiFePO$_4$ Nanoparticles During Battery Discharge. *Nano Lett.* **2011**, *11*, 4890−4896.

(18) Cogswell, D. A.; Bazant, M. Z. Coherency Strain and the Kinetics of Phase Separation in LiFePO$_4$ Nanoparticles. *ACS Nano* **2012**, *6*, 2215−2225.

(19) Bazant, M. Z. Thermodynamic stability of driven open systems and control of phase separation by electro-autocatalysis. *Faraday Discuss.* **2017**, *199*, 423−463.

(20) Bai, P.; Bazant, M. Z. Charge transfer kinetics at the solid-solid interface in porous electrodes. *Nat. Commun.* **2014**, *5*, 3585.

(21) Xin, Y.-M.; et al. A Review on Application of LiFePO$_4$ based composites as electrode materials for Lithium Ion Batteries. *Int. J. Electrochem. Sci.* **2021**, *16*, 210655.

(22) Malik, R.; Abdellahi, A.; Ceder, G. A Critical Review of the Li Insertion Mechanisms in LiFePO$_4$ Electrodes. *J. Electrochem. Soc.* **2013**, *160*, A3179−A3197.

(23) Zhou, F.; Kang, K.; Maxisch, T.; Ceder, G.; Morgan, D. The electronic structure and band gap of LiFePO$_4$ and LiMnPO$_4$. *Solid State Commun.* **2004**, *132*, 181−186.

(24) Xiao, P.; Henkelman, G. Kinetic Monte Carlo Study of Li Intercalation in LiFePO$_4$. *ACS Nano* **2018**, *12*, 844−851.

(25) Kang, B.; Ceder, G. Battery materials for ultrafast charging and discharging. *Nature* **2009**, *458*, 190−193.

(26) Chen, G., Song, X., Richardson, T. J. Metastable Solid-Solution Phases in the LiFePO$_4$/FePO$_4$ System. *J. Electrochem. Soc.* **2007**, *154*, A627.

(27) Allen, J. L.; Jow, T. R.; Wolfenstine, J. Kinetic Study of the Electrochemical FePO$_4$ to LiFePO$_4$ Phase Transition. *Chem. Mater.* **2007**, *19*, 2108−2111.

(28) Allen, J. L.; Jow, T. R.; Wolfenstine, J. Analysis of the FePO$_4$ to LiFePO$_4$ phase transition. *J. Solid State Electrochem.* **2008**, *12*, 1031−1033.

(29) Zhu, C.; et al. Size-Dependent Staging and Phase Transition in LiFePO$_4$/FePO$_4$. *Adv. Funct. Mater.* **2014**, *24*, 312−318.

(30) Zhang, W.-J. Structure and performance of LiFePO$_4$ cathode materials: A review. *J. Power Sources* **2011**, *196*, 2962−2970.

(31) Love, C. T.; et al. Review of LiFePO$_4$ Phase Transition Mechanisms and New Observations from X-ray Absorption Spectroscopy. *J. Electrochem. Soc.* **2013**, *160*, A3153−A3161.

(32) Moškon, J., Krizan, G., Dominiko, R., Gaberšček, M. "Steady-State" and "Activated" State in Li Ion Insertion Systems. In *ECS Meeting Abstracts* vols MA2015-03 575; The Electrochemical Society, 2015.

(33) Katrašnik, T.; et al. Entering Voltage Hysteresis in Phase Separating Materials: Revealing the Electrochemical Signature of the Intraparticle Phase Separated State. *Adv. Mater.* **2023**, *35*, 2210937.

(34) Liu, Q.; et al. Rate-Dependent, Li-Ion Insertion/Deinsertion Behavior of LiFePO$_4$ Cathodes in Commercial 18650 LiFePO$_4$ Cells. *ACS Appl. Mater. Interfaces* **2014**, *6*, 3282−3289.

(35) Fey, G. T.-K.; Chen, Y. G.; Kao, H.-M. Electrochemical properties of LiFePO$_4$ prepared via ball-milling. *J. Power Sources* **2009**, *189*, 169−178.

(36) Gaberscek, M.; Dominko, R.; Jamnik, J. Is small particle size more important than carbon coating? An example study on LiFePO$_4$ cathodes. *Electrochem. Commun.* **2007**, *9*, 2778−2783.

(37) Cogswell, D. A.; Bazant, M. Z. Size-dependent phase morphologies in LiFePO$_4$ battery particles. *Electrochem. Commun.* **2018**, *95*, 33−37.

(38) Wagemaker, M.; Mulder, F. M.; Van der Ven, A. The Role of Surface and Interface Energy on Phase Stability of Nanosized Insertion Compounds. *Adv. Mater.* **2009**, *21*, 2703−2709.

(39) Li, D.; Liu, X.; Zhou, H. The Size-Dependent Phase Transition of LiFePO$_4$ Particles during Charging and Discharging in Lithium-Ion Batteries. *Energy Technol.* **2014**, *2*, 542−547.

(40) Malik, R.; Zhou, F.; Ceder, G. Kinetics of non-equilibrium lithium incorporation in LiFePO$_4$. *Nat. Mater.* **2011**, *10*, 587−590.

(41) Li, Y.; et al. Phase-field simulation tending to depict practical electrodeposition process in lithium-based batteries. *Chin. Chem. Lett.* **2023**, *34*, 107993.

(42) Bazant, M. Z. Theory of Chemical Kinetics and Charge Transfer based on Nonequilibrium Thermodynamics. *Acc. Chem. Res.* **2013**, *46*, 1144−1160.

(43) Smith, R. B.; Khoo, E.; Bazant, M. Z. Intercalation Kinetics in Multiphase-Layered Materials. *J. Phys. Chem. C* **2017**, *121*, 19.

(44) Bartelt, N. C.; et al. Simple Stochastic Model of Multiparticle Battery Electrodes Undergoing Phase Transformations. *Phys. Rev. Appl.* **2018**, *10*, 044056.

(45) Gomadam, P. M.et al. Modeling Li/CF$_x$-SVO Hybrid-Cathode Batteries. *J. Electrochem. Soc.* **2007**, *154*, A1058.

(46) Liang, Q.; Bazant, M. Z. Hybrid-MPET: an open-source simulation software for hybrid electrode batteries. 2023, 2305.15599. arXiv. http://arxiv.org/abs/2305.15599 (accessed 12/14/2023).

(47) Kuo, J. J.; Kang, S. D.; Chueh, W. C. Contact Resistance of Carbon-Li$_x$ (Ni,Mn,Co)O$_2$ Interfaces. *Adv. Energy Mater.* **2022**, *12*, 2201114.